Remotely Detected MRI Velocimetry in Microporous Bead Packs
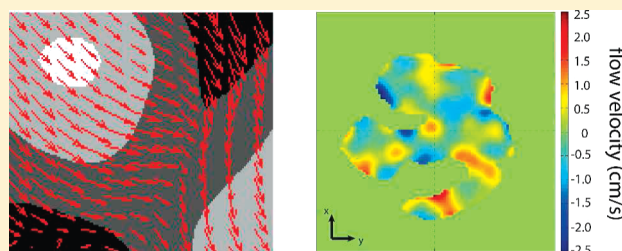
Nicholas W. Halpern-Manners, Jeffrey L. Paulsen,[†] Vikram S. Bajaj,[*] and Alexander Pines

Materials Sciences Division, Lawrence Berkeley National Laboratory & Department of Chemistry, University of California, Berkeley, Berkeley, California 94720, United States

S *Supporting Information*

ABSTRACT: Many NMR and MRI methods probe fluid dynamics within macro- and mesoporous materials, but with few exceptions, they report on its macroscopically averaged properties. MRI methods are generally unable to localize microscopic features of flow within macroscopic samples because the fraction of the enclosing detector volume occupied by these features is so small. We have recently overcome this problem using remotely detected MRI velocimetry, a technique in which spatial, chemical, and velocity information about elements of the flow is encoded with a conventional NMR coil and detected

sensitively at the sample outflow by a volume-matched microdetector. Here, we apply this method to microporous model systems, recording MRI images that correlate local velocity, spin relaxation, and time-of-flight in microscopic resolution and three spatial dimensions. Our results illustrate that remotely detected MRI is an effective approach to elucidate flow dynamics in porous materials including bead pack microreactors and chromatography columns.

■ INTRODUCTION

Nuclear magnetic resonance spectra of liquid samples are profoundly sensitive to both coherent and incoherent motion of the constituent spins.[1,2] Further, through their dependence on the average local molecular environment, NMR spectra can directly encode information about chemistry and chemical dynamics in multiphasic or multicomponent ensembles without labeling or perturbative modification of the analytes. Finally, NMR, in combination with spatially varying magnetic field gradients, provides chemically rich images deep within optically opaque structures, materials, and organs. These advantages of MRI over other dynamical fluid imaging techniques[3−5] explain why MRI remains a vital technique in applications as diverse as clinical angiography and oil well logging.

A wide variety of NMR methods have been developed in order to probe fluid properties within macro- and mesoporous materials. The majority of these studies report ensemble properties of the flow, including diffusion, relaxation, and the flow propagator,[6,7] averaged over the extent of the macroscopic sample. While these studies have provided information about dispersion,[8−10] surface relaxivity,[11] wettability,[12] permeability,[13,14] pore size,[15−17] and velocity,[8] they typically cannot directly localize features of the flow within the larger sample, because the fraction of the enclosing detector volume occupied by the sample is so small. Efforts to spatially resolve flowing fluids[18−22] in porous media are thus limited in their resolution, necessitating the use of larger representative model systems and often employing voxel sizes on the order of or larger than the pores themselves. These difficulties act to conceal the intricate pore distributions and flow properties found in complex porous samples at relevant scales.

Our particular interest is to expand the capabilities of MRI flow imaging to a regime of microscopic detail for which the inherently low sensitivity renders it poorly suited. The microscopic details of a macroscopic object might be most sensitively imaged if one could implant, within it, NMR detectors that precisely enclose each feature of interest. This is, however, impractical in most cases and impossible in systems whose internal structures are intrinsically inaccessible to a local detector. We instead employ remote detection,[23,24] a technique that spectroscopically mimics the implantation of a volume-matched detector around a microscopic feature.[25] In remotely detected MRI, conventional MRI phase encoding sequences are applied to encode velocimetric, chemical, and spatial information into the spin degrees of freedom of the flowing analyte using an encoding coil that contains the entire sample. Next, the information is stored as longitudinal magnetization (intensity along the applied field) for travel to an optimized microsolenoid detector at the sample outflow. Within the detector, the information is read out stroboscopically and the data reconstructed by simple Fourier transformation, yielding not just an image but also a correlated time-of-flight dimension that reflects fluid transport from the encoding region to the detector. The order of arrival of the fluid packets is independent of spatial encoding and therefore does not influence the appearance of the image. Because the volume of the
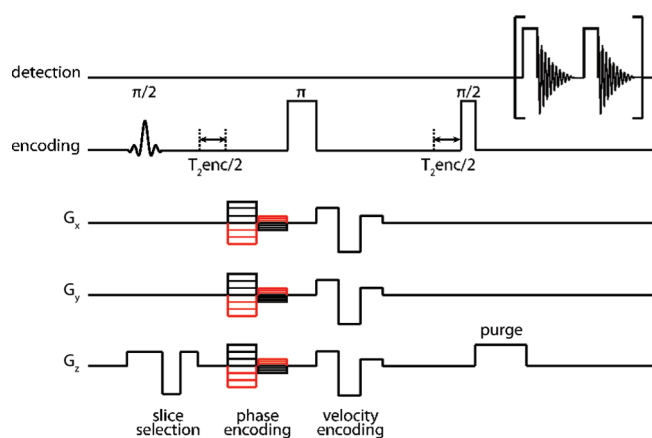
Figure 1. Pulse sequence for multidimensional remotely detected imaging experiments, shown with optional velocity and relaxation encoding steps. Following the initial slice-selective excitation, information regarding the position, velocity, and relaxation properties of the fluid may be encoded in the phase of the spins. Information is stored along the longitudinal axis for transport to a microcoil detector, where it is read off stroboscopically to provide an additional time-of-flight dimension.

microcoil is approximately matched to the volume of the voxels in the imaging experiment, we realize a dramatically enhanced filling factor for detection; further, because we detect the fluid in an environment free from magnetic susceptibility broadening, we obtain excellent linewidths. Combined, these improve the sensitivity by up to several orders of magnitude compared to conventional imaging in a similar geometry.[26]

In other studies, we have applied remote detection in flow imaging and velocimetry of liquids within microfluidic devices[25,27−30] and membranes,[31] as well as gas flow within macro-[32] and meso-porous[33] materials. Here, we extend the method to flow imaging, velocimetry, and relaxometry of liquid flow within porous bead packs, an initial application of remotely detected velocimetry techniques outside the realm of regular microfluidic flow. In addition to their use as microreactors, such bead packs are ubiquitous model systems for many investigations of flow in porous media, including rocks, sand, membranes, and biofilms. We acquire images of water flowing through packed beads with diameters ranging from 150 to 600 μm, obtaining spatial resolutions as low as 45 μm, smaller than in any previous porous media MR imaging experiment. To record these images, we employ MRI experiments that measure flow and diffusion through the application of magnetic field gradient pulses that render the NMR phase sensitive to position or velocity alone.[6] A series of such experiments with velocity encoding gradients applied along orthogonal axes reconstructs a Eulerian vector flow field. Since the spatial resolution of all MRI images is limited by the nonrefocusable dispersion during the encoding time, we use gradient moment nulling methods to compensate for the deleterious effects of spin motion.[34]

An example of a remote detection pulse sequence with velocity encoding is shown in Figure 1. In the context of a spin echo sequence, our experiment begins with slice selective excitation, which is followed by spatial phase encoding, optional velocity or T_2 encoding, storage along the longitudinal axis, transport to the microcoil detector, and stroboscopic detection. For a detailed explanation of remote imaging and velocimetry experiments, as well as a schematic of the remote detection experiment, see the supporting material for ref 25.

■ EXPERIMENTAL METHODS

Bead Pack. The packed bead flow systems were contained in enclosing Teflon cylinders with microfluidic connectors on each end (Upchurch Scientific). The diameters of the coarse and fine bead pack bores were approximately 2 and 1.6 mm, respectively. The bores were filled with glass beads (Sigma-Aldrich) with diameters ranging from 150 to 212 μm for the fine pack and 425−600 μm for the coarse pack. While the beads were not fixed by sintering or chemical adhesion, our relatively slow flow rates ensured that they were not fluidized and that they reached equilibrium positions in a very short time. Following passage through the porous encoding region, fluid traveled to the microcoil detector through a short length of 150 μm ID PEEK microcapillary tubing, driven by regulated, pressure-based flow. For the high-resolution experiments with size 64 × 64 × 64 (16-fold subsampled, as described *vide infra*), we attained a voxel size of 54 μm × 54 μm × 89 μm for the coarse bead pack (FOV$_{x,y}$ = 3.45 mm, FOV$_z$ = 5.72 mm) and 45 μm × 45 μm × 53 μm for the fine bead pack (FOV$_{x,y}$ = 2.90 mm, FOV$_z$ = 3.40 mm).

Experimental Setup. The remote detection experiments were performed with a 7.05 T Oxford Instruments wide bore magnet and a Varian imaging console. Excitation and storage pulses were performed with a 40 mm Varian volume imaging probe, while gradients were applied using a Varian triple-axis gradient system producing up to 100 G/cm on all three axes. The detection probe was a custom-built microcoil probe connected to the capillary tubing via commercially available connectors (Upchurch Scientific). Water flowed through the system at constant pressures of 18 and 50 psi (coarse and fine bead packs, respectively), driven by a nitrogen gas ballast system and monitored by a proportional control setup (Omega Engineering).

Pulse Sequence. The pulse sequence for remote detection (shown in Figure 1) consisted of a slice selective $\pi/2$ excitation (typically, a sinc pulse with 5 kHz bandwidth), followed by two- or three-dimensional phase encoding (1−1.5 ms). Slice selection and phase encoding gradients were balanced in order to cancel phase evolution due to motion of the spins.[34] Refocusing of transverse magnetization occurred via a π pulse, and a final $\pi/2$ pulse was applied after the proper echo delay in order to store the encoded magnetization along $\hat{z}$ for transport to the detection coil. When used, two- or three-lobe velocity-encoding gradients, designed to null the phase accrued due to the position (and, if three-lobed, the acceleration) of spins and encode only the velocity, were applied before the storage pulse, with a total duration of 1−1.5 ms. T_2 encoding was performed via a set of experiments with an additional delay symmetrically incremented about the refocusing pulse. Phase cycling was employed to store each component of the magnetization and to filter out any signal from spins outside of the encoding region.

Subsampling. Compressed sensing methods were used in the acquisition of the three-dimensional data sets, following a methodology detailed in a previous work.[35] In brief, k-space sampling took place according to a predetermined subsampling mask, chosen to give an accurate representation of the data after transformation and reconstruction in a sparse wavelet domain. Experiments with 32 × 32 × 32 resolution used a k-space mask with 8-fold subsampling (∼12 h acquisition time), while the data taken with 64 × 64 × 64 resolution were subsampled by a factor of 16 (∼55 h). For further details regarding the generation of subsampling masks, transformation between k-space, real, and sparse domains, and reconstruction, please see ref 34.
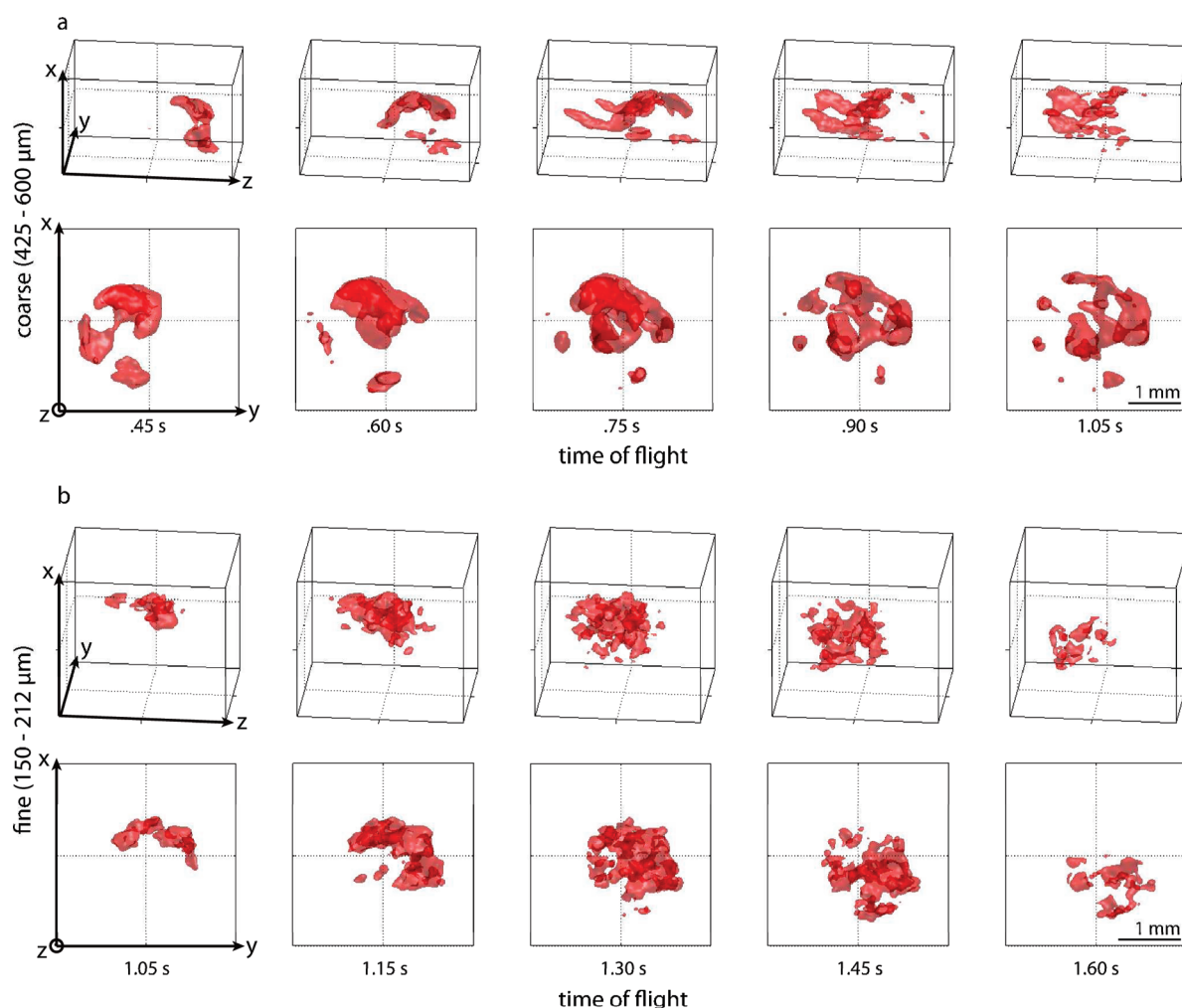
Figure 2. High resolution time-of-flight images of flow through both coarse (a) and fine (b) bead packs. 3D isosurfaces of signal intensity are shown at five representative TOF points, in both isometric and axial points of view. The imaging resolution was $64 \times 64 \times 64$ with 16-fold subsampling, yielding voxel dimensions of $54\,\mu m \times 54\,\mu m \times 89\,\mu m$ for the coarse bead pack ($FOV_{x,y} = 3.45$ mm, $FOV_z = 5.72$ mm) and $45\,\mu m \times 45\,\mu m \times 53\,\mu m$ for the fine bead pack ($FOV_{x,y} = 2.90$ mm, $FOV_z = 3.40$ mm). Movies of these data (across the time-of-flight dimension) are available in .avi format as Supporting Information.

Data Processing. All data were processed using Matlab (Mathworks). Following apodization and Fourier transformation of the direct dimension, the water resonance is integrated to obtain complex-valued data for the indirect phase-encoded dimensions of the experiment. For data acquired with compressed sensing, the images are first reconstructed by a nonlinear L1 minimization scheme that seeks to maintain the agreement of the image model with experimental data and maximize the sparsity of the image model that agrees with the experimental data.[36] All of the acquired data sets are apodized by Gaussian functions centered at the origin of k-space, zero-filled by a factor of 3, and transformed by a multidimensional Fourier transform to obtain the complex image.

Images containing a velocity-encoding dimension were processed as described above, followed by determination of the phase difference between two images taken with velocity gradient pulses of opposite sign, to yield velocity data. The repetition of this procedure along three orthogonal axes yields a Eulerian (vector) flow field in each voxel. All image information is also correlated to a Lagrangian description of the flow, expressed in the particle frame by the correlated time-of-flight dimension.

T_2 values were obtained by fitting a monoexponential decay in each voxel to a series of experiments with incremented T_2-encoding delay. Velocity and T_2 data were masked by eliminating voxels with signal intensity less than the maximum intensity multiplied by a cutoff value.

■ RESULTS

Time-of-Flight Images of Flow. We obtained high-resolution time-of-flight images of flow through both coarse ($425-600$ μm diameter) and fine ($150-212\,\mu m$ diameter) bead packs at $64 \times 64 \times 64$ resolution (with 16-fold subsampling). Surface plots of the fluid distribution within coarse (Figure 2a) and fine (Figure 2b) bead packs are shown in isometric and head-on views for five representative time-of-flight points, and movies of the flow may be found in the Supporting Information. Fluid flows from left to right, with liquid closest to the bead pack outlet, or liquid following comparatively rapid flow lines, arriving first at the detector. As longer TOF points are sampled, we see flow from regions farther from the outlet and from areas with slower or more restricted flow. Fluid from stagnant flow regions may not
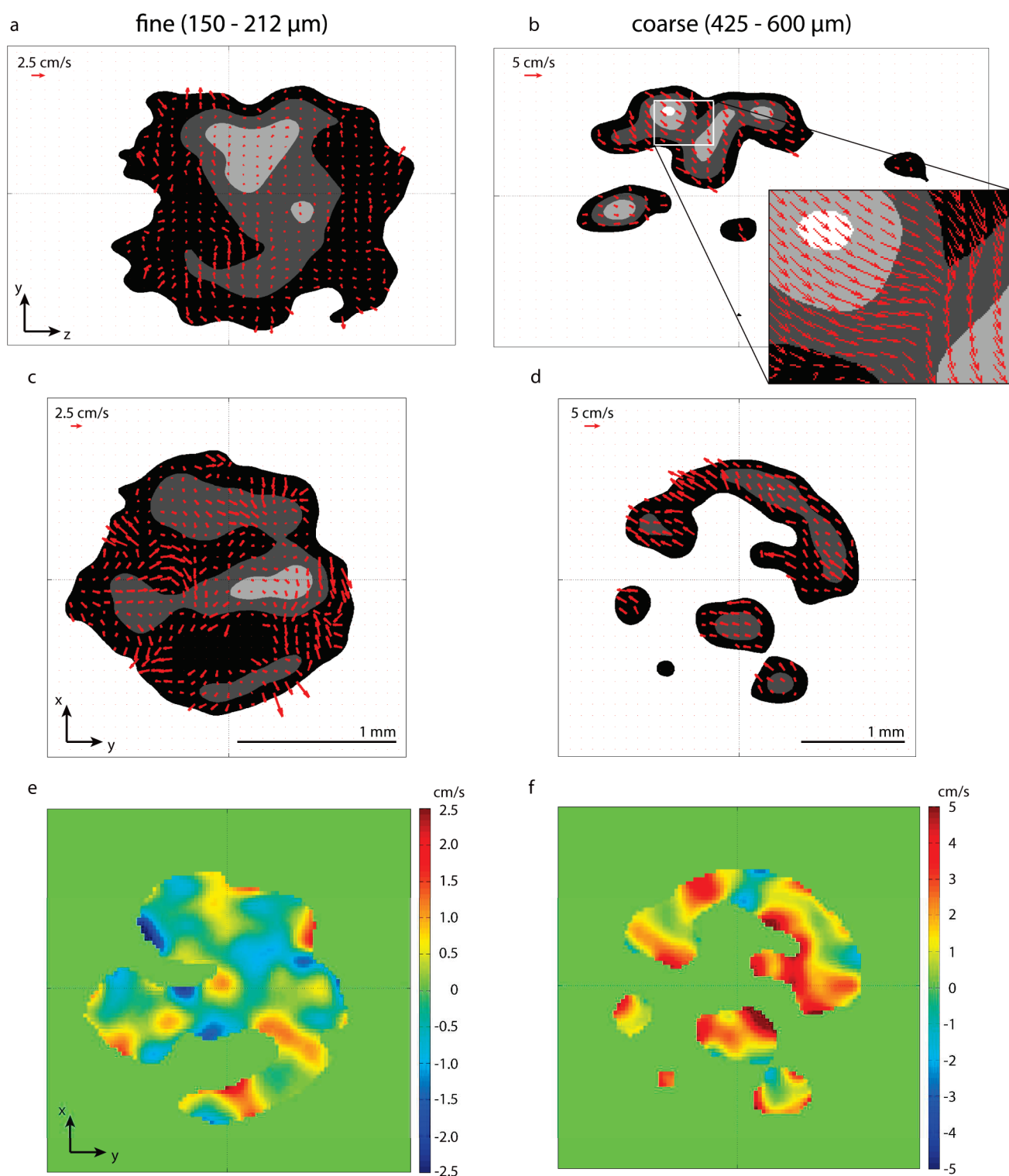
4025

dx.doi.org/10.1021/jp109728j |*J. Phys. Chem. A* 2011, 115, 4023–4030

Figure 3. Selected 2D slices of the 3D velocimetric data for each bead pack. Intensity contours are drawn parallel (a, b) and orthogonal (c, d) to the direction of flow for a selected time-of-flight point in each data set, overlaid with 2D in-plane velocity vectors. The velocity component along the direction of flow (V_z) is shown for the chosen axial slices in parts e and f.

reach the detector before spin—lattice relaxation erases the encoding information, and therefore, our time-of-flight images may understate their contribution to the overall flow dynamics. The void space within the remote images may correspond either to the beads themselves or to areas with slow-moving flow. The

beads themselves do not contribute to the flowing signal, and therefore, their positions cannot be directly inferred.

Velocity-Encoded Images. MR images can be sensitized to motion by the addition of magnetic field gradient waveforms that cause signal phase to depend on velocity, while nulling its dependence
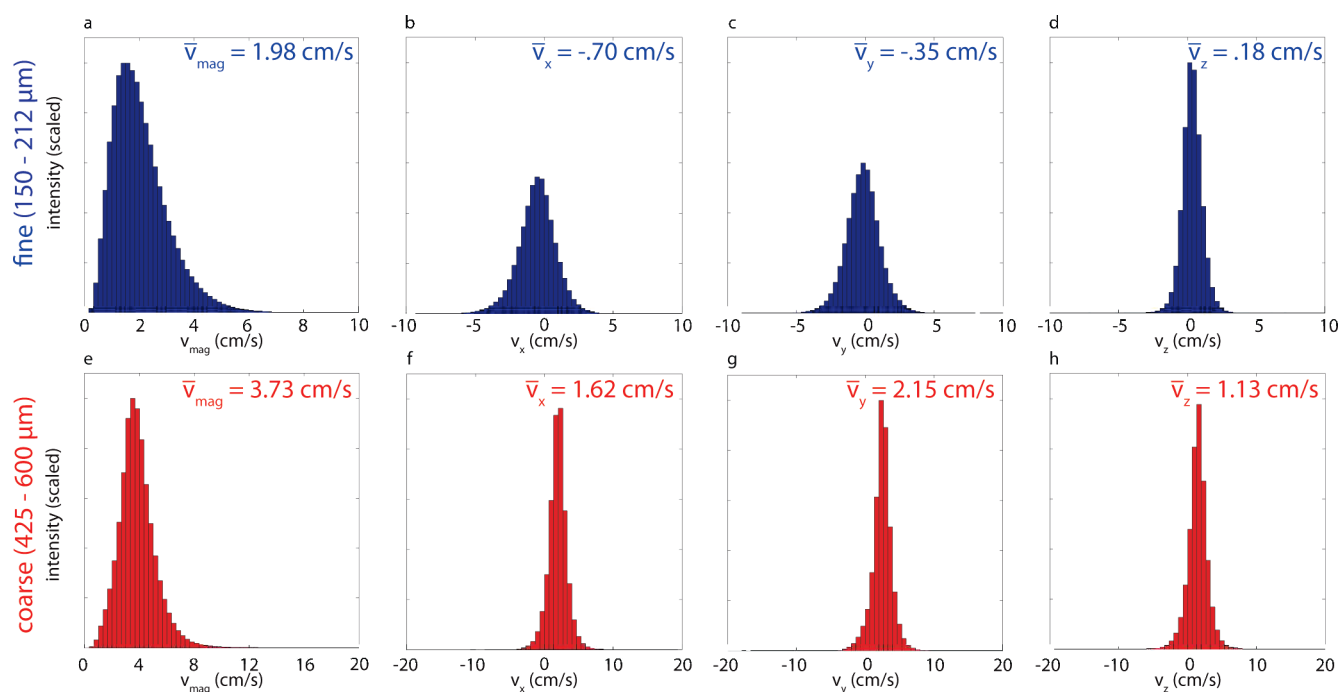
Figure 4. Intensity-weighted histograms for each velocity component and the overall velocity magnitude, for fine (a−d) and coarse (e−h) bead packs. Average velocities for each histogram are noted, and the overall intensity of each bin is scaled to the maximum bin within its respective bead pack. Weighting each velocity by the signal intensity in that voxel serves to correct inaccuracies due to variations in fluid density.

on position or acceleration. This has been previously demonstrated in remote detection experiments performed with microfluidic devices.[25] The phase generated by motion of nuclei through these gradients allows for direct measurement of each velocity component, when normalized to a control experiment in which the sign of the gradient lobes has been inverted. In Figure 3, we show several two-dimensional velocity plots for a single time-of-flight, in both coarse and fine bead packs. In parts a and b, we see contour plots chosen so that the slice is in the xz-plane, parallel to the direction of flow, with two-dimensional in-plane velocity vectors. Axial (xy) slices from the same time-of-flight are shown with transverse velocity vectors in parts c and d, while the z-component of velocity is shown in parts e and f.

While the velocity vectors are generally inclined toward the direction of flow in both bead packs, the distribution of flow in the fine bead pack is far more complex. The axial V_z plot shows substantial regions of retrograde flow, while the parallel plot illustrates large regions of circulatory flow. By contrast, flow through the coarse bead pack is quite straightforward and is primarily confined to several large flow paths. Due to the irregularity of the bead structure, the flow pathways are not necessarily symmetric about the axis of flow. As can be seen in Figure 2, fluid in the fine bead pack undergoes a net displacement along the x-axis while the distribution in the coarse bead pack clearly shifts along the y-axis, observations which are confirmed and characterized by examining per-voxel distributions of velocity.

In Figure 4, we show histograms of velocity distributions for both coarse and fine bead pack data. The complex velocity-encoded images were summed over the time-of-flight dimension (for points containing encoded spins), and the phase difference was found for each voxel. Finally, the data were weighted by the signal intensity for each fluid-containing voxel. The amplitudes of the velocity component histograms are scaled to the largest bin for their respective bead pack. In the coarse bead pack (red,

bottom row), the distributions for V_x (f) and V_y (g) are noticeably shifted toward a nonzero mean, consistent with asymmetric flow pathways discussed above. The distribution of flow pathways in relevant porous media samples is likely to be similarly nonuniform, and the combination of velocity data (Eulerian) and time-of-flight images (Lagrangian) is particularly well-suited to elucidate irregular flow pathways.

In parts d and h, we show the fine and coarse bead pack velocity histograms for V_z, the component along the flow direction. The nonzero mean corresponds to a net movement of spins in the direction of flow, although the distributions also include negative velocities which may indicate the effects of reversed flow and recirculation,[20] dispersion, and tortuosity.

The histograms of velocity magnitude are shown in parts a and e. When comparing the widths of the histograms relative to their means, the fine bead pack histogram demonstrates a wider range of relative velocities, as would be expected for the increased dispersion within the smaller pore network. However, further conclusions regarding the comparative velocities within each porous region cannot be easily drawn in these circumstances, due to the differences in phantom construction and experimental conditions.

T_2-**Encoded Images.** A separate series of three-dimensional experiments involved an incremented T_2-encoding delay applied symmetrically about the refocusing pulse, as indicated in Figure 1. We fit the T_2 decay curves for each voxel using experiments with additional T_2 encoding delays of 0, 3, 6, and 9 ms (on top of the ∼2−4 ms remote encoding period), shown in Figure 5 for three slices within a single time-of-flight in both coarse (425−600 μm diameter) (a) and fine (150−212 μm diameter) (b) bead packs. The T_2 values typically vary from ∼1 to 20 ms, and are generally smaller within the fine bead pack. While our goal is to demonstrate that the remote detection experiment is well-suited to measure T_2 relaxation, analysis of the underlying factors and their
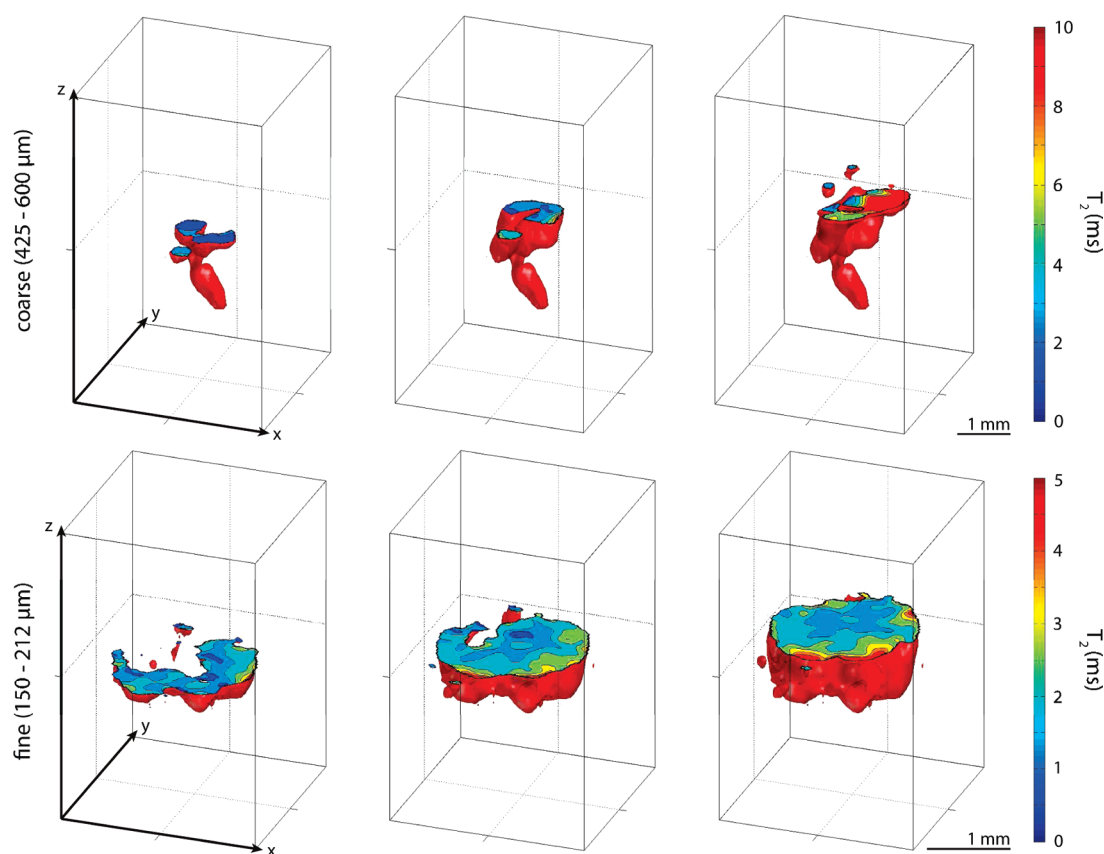
4027

dx.doi.org/10.1021/jp109728j |*J. Phys. Chem. A* 2011, 115, 4023–4030

Figure 5. T_2 relaxation data for fluid flow within coarse and fine bead packs, as indicated adjacent to the figure axis labels. Isosurface contours of the flow volume are shown for a single time-of-flight, truncated at three representative planes within the sample in order to illustrate the relaxation values within the pore structure. Relaxation values were obtained by performing a per-voxel fit of signal intensity for a series of images with incremented T_2-encoding delays.

relative significance is not straightforward, and our discussion below will be limited to a short overview of these concerns.

■ DISCUSSION

Previous studies of flow within porous media have established that there is a large heterogeneity in fluid and velocity distributions. Some pores exhibit evidence of stagnant flow, while others contain fluid flowing with velocities several times greater than the bulk flow.[18,22] A relatively small fraction of pores may conduct a significant fraction of the fluid.[21] Variations in fluid channeling and velocity distributions within porous media arise from a combination of the effects of local pore structure and the overall topology of the porous network. Because of these channeling effects, the fluid shown in Figure 2 may, in the extreme case, represent only the primary pathways which allow for rapid, relatively unobstructed flow. Fluid trapped in obstructed or stagnant regions may not travel to the detector in a time shorter than the phase memory of the spins, making it difficult to distinguish between stagnant regions, from which encoded flow never reaches the detector, and the glass beads, from which flow is excluded. Thus, our inability to apply direct imaging at this scale restricts us from obtaining a void-space image of the bead pack.

However, it is impossible to apply conventional MR imaging methods with pore-scale resolution in many interesting porous media. Most porous media and the flows they conduct are far less homogeneous and regular than any model bead pack, both in

structure and fluid composition. While the dynamics of monophasic flow through a stationary bead pack scale with the dimensionless Reynolds number, multiphasic flows observe more complex scaling laws; experimental models, therefore, that simply scale their dimensions to the point where conventional MRI can be applied will fail to capture the relevant fluid dynamics. Further, many materials for which MRI might be useful, such as microporous rocks, membranes, or aerogels, either occur naturally or are synthesized with a pore scale that is relevant for their function and cannot be emulated by a model system. Remotely detected MRI allows us to avoid these tenuous scaling conversions by performing experiments directly upon the sample of interest (although the efficiency of the experiment may be compromised when examining very slow flow within naturally occurring porous media). Even in systems with larger pores, in which direct imaging can be applied, remote detection is able to provide a complementary time-of-flight (Lagrangian) view of the flow field.

In microporous systems, ours is one of the few methods that can provide simultaneous and correlated descriptions of the flow field in terms of Eulerian local velocities and Lagrangian times of flight. Statistical analyses of the velocity distributions show that fluid within the fine bead pack has a wider distribution of velocities (relative to the distribution mean), consistent with a greater level of dispersion within the more tightly packed phantom. The velocimetry data indicate the significant presence of dispersive and retrograde flow, particularly in the fine bead

pack. This behavior is clearly illustrated by the large regions of negative axial flow in Figure 3f, the circulatory behavior of the flow vectors in Figure 3d, the increased relative histogram widths, and the significant number of negative velocity components in the histograms.

In addition to the advantages in scale and flexibility already described, remotely detected velocimetry is less susceptible to inaccuracies in measured data. Specifically, partial volume effects can arise when the size of an imaging voxel is comparable to the pore size or even larger.[18] In that case, the phase accrued in each voxel is the intensity-weighted, phase space geometric sum of all components within the voxel and not the average velocity in the voxel. Remote detection allows us to use much smaller imaging voxels and is additionally sensitive only to flowing spins, with the result that the experimentally determined phase contrast more accurately reflects the mean velocity of flowing fluid within each voxel. In our measurements, for example, the velocities within the coarse bead pack should be largely free of partial volume effects, as the voxel dimensions are at least a factor of 2 lower than the bead radii. However, average velocities may be slightly overestimated in situations where there are stagnant or very slow moving volumes of flow which do not reach the detector in a reasonable time.

Finally, in addition to obtaining velocimetry data within the porous bead packs, we demonstrate the acquisition of transverse relaxation data. We depict these not as T_2-weighted images but as images in which we have fit the T_2 in each voxel through a series of measurements. There are two primary causes of T_2 relaxation in porous media: surface relaxation due to dipolar interactions[37] and paramagnetic impurities,[38] and dispersion through gradients in the internal field caused by the solid−liquid interface throughout the sample.[39−46] In situations where surface relaxation dominates, T_2 can be used as a direct probe of the surface area-to-volume ratio of the pores, and thus a measurement of the pore size distribution.[47] It should be noted that the effects of magnetic susceptibility heterogeneity increase in proportion to the static magnetic field strength. Therefore, after a certain point, diffusion through the internal field can substantially interfere with the determination of pore size distributions.[48] While a detailed analysis is beyond the scope of our work, we observe several trends. First, T_2 within the fine bead pack is, on average, smaller than in the coarse bead pack. This might be related both to an increase in surface relaxation with smaller pore size as well as to larger magnetic field gradients within the finer porous structure. Similarly, the T_2 map within the coarse bead pack indicates larger T_2 values within larger regions of flow, which could be related to a decrease in the influence of surface relaxation as well as weaker internal field gradients near the pore center and a smaller flow rate through these gradients. Since we performed these experiments at relatively high field, susceptibility gradients are likely to dominate. While a direct (i.e., not remotely detected) measurement of the spatially resolved T_2 values within these bead packs would be a worthwhile comparison, such an experiment would take a prohibitively long time due to the severely reduced filling factor in this microporous sample. However, previous bulk experiments using a saturated sandstone core (with pore sizes of 50 μm or less) have shown discrete T_2 distributions ranging from 0.2 to 32.6 ms,[49] in good agreement with our remotely detected values. We further note that remote detection can permit T_2 measurements at arbitrary field strengths (*vide infra*) because the flowing analyte can be polarized in a high magnetic field before it enters the sample chamber, in which it can then be encoded in any given magnetic field.

We have demonstrated a generic method for magnetic resonance velocimetry and imaging of flow within microporous materials. We are presently applying the technique to study multiphasic flow and small molecule separations within microchromatographic columns, and anticipate its extension to multicomponent systems including microreactors and confined combustion devices.[50] In these experiments, chemical shift information may be encoded in indirect spectral dimensions or detected in the direct dimension after flow to the microcoil, allowing the flow volumes associated with each signal component to be isolated and localized within the porous structure. More importantly, because remote detection separates the polarization, detection, and encoding steps of the experiment, it will enable a new variety of portable flow profiling devices for use in rock core sample characterization and online industrial process monitoring. For example, prepolarization of the fluid can occur in the inhomogeneous field of a permanent magnet, and the fluid can be then transported to a region of arbitrary magnetic field in which spatial and other encoding can take place, after which the result can be detected inductively or by a microfabricated magnetometer that operates without a magnetic field.[51,52] Such a geometry would also provide greater sample access and thus lend itself to multimodal (X-ray computed tomography, optical) imaging schemes.

■ CONCLUSIONS

We have applied remotely detected imaging, velocimetry, and relaxometry toward microporous bead packs. The sensitivity enhancements characteristic to remote detection allow us to perform high-resolution experiments on porous media which would be inaccessible to typical detection techniques. The combination of time-of-flight and velocimetry data provides complementary views of the fluid flow within the pore structure, and allows for clear visualization of the dominant flow pathways and dispersive fluid behavior. Finally, we probe the T_2 relaxation of fluid within the bead packs, obtaining data which provides further insight into the properties of the complex porous environment.

■ ASSOCIATED CONTENT

Ⓢ Supporting Information. Movies (.avi format) of high-resolution (64 × 64 × 64) time-of-flight resolved fluid flow through both fine and coarse bead packs, corresponding to the full data sets used in Figure 2. This material is available free of charge via the Internet at http://pubs.acs.org.

■ AUTHOR INFORMATION

Corresponding Author
*E-mail: vsbajaj@lbl.gov, vikbajaj@gmail.com. Telephone/fax: (510)-642-2094/(510)-666-3768.

Present Addresses
†Schlumberger-Doll Research, One Hampshire St, Cambridge MA, 02139.

■ ACKNOWLEDGMENT

■ REFERENCES

(1) Hahn, E. L. *Phys. Rev.* **1950**, *80*, 580.

(2) Abragam, A. *Principles of Nuclear Magnetism*; Clarendon Press: Oxford, U.K., 1961.

(3) Abbiss, J. B.; Chubb, T. W.; Pike, E. R. *Opt. Laser Technol.* **1974**, *6*, 249.

(4) Adrian, R. J. *Annu. Rev. Fluid Mech.* **1991**, *23*, 261.

(5) Ketcham, R. A.; Carlson, W. D. *Comput. Geosci.* **2001**, *27*, 381.

(6) Callaghan, P. T. *Principles of nuclear magnetic resonance microscopy*; Clarendon Press: Oxford, U.K., 1991.

(7) Song, Y. Q.; Cho, H.; Hopper, T.; Pomerantz, A. E.; Sun, P. Z. *J. Chem. Phys.* **2008**, *128*, 052212.

(8) Seymour, J. D.; Callaghan, P. T. *AIChE J.* **1997**, *43*, 2096.

(9) Khrapitchev, A. A.; Callaghan, P. T. *Phys. Fluids* **2003**, *15*, 2649.

(10) Hunter, M. W.; Callaghan, P. T. *Phys. Rev. Lett.* **2007**, *99*, 210602.

(11) Hurlimann, M. D.; Latour, L. L.; Sotak, C. H. *Magn. Reson. Imaging* **1994**, *12*, 325.

(12) Howard, J. J. *Magn. Reson. Imaging* **1998**, *16*, 529.

(13) Banavar, J. R.; Schwartz, L. M. *Phys. Rev. Lett.* **1987**, *58*, 1411.

(14) Pape, H.; Arnold, J.; Pechnig, R.; Clauser, C.; Talnishnikh, E.; Anferova, S.; Blumich, B. *Pure Appl. Geophys.* **2009**, *166*, 1125.

(15) Liaw, H. K.; Kulkarni, R.; Chen, S. H.; Watson, A. T. *AIChE J.* **1996**, *42*, 538.

(16) Mair, R. W.; Wong, G. P.; Hoffmann, D.; Hurlimann, M. D.; Patz, S.; Schwartz, L. M.; Walsworth, R. L. *Phys. Rev. Lett.* **1999**, *83*, 3324.

(17) Song, Y.-Q. *Concepts Magn. Reson., Part A* **2003**, *18A*, 97.

(18) Feinauer, A.; Altobelli, S. A.; Fukushima, E. *Magn. Reson. Imaging* **1997**, *15*, 479.

(19) Johns, M. L.; Sederman, A. J.; Bramley, A. S.; Gladden, L. F.; Alexander, P. *AIChE J.* **2000**, *46*, 2151.

(20) Kutsovsky, Y. E.; Scriven, L. E.; Davis, H. T.; Hammer, B. E. *Phys Fluids* **1996**, *8*, 863.

(21) Sederman, A. J.; Johns, M. L.; Alexander, P.; Gladden, L. F. *Chem. Eng. Sci.* **1998**, *53*, 2117.

(22) Sederman, A. J.; Johns, M. L.; Bramley, A. S.; Alexander, P.; Gladden, L. F. *Chem. Eng. Sci.* **1997**, *52*, 2239.

(23) Moule, A. J.; Spence, M. M.; Han, S. I.; Seeley, J. A.; Pierce, K. L.; Saxena, S.; Pines, A. *Proc. Natl. Acad. Sci. U.S.A.* **2003**, *100*, 9122.

(24) Granwehr, J.; Harel, E.; Han, S.; Garcia, S.; Pines, A.; Sen, P. N.; Song, Y. Q. *Phys. Rev. Lett.* **2005**, *95*, 075503.

(25) Bajaj, V. S.; Paulsen, J.; Harel, E.; Pines, A. *Science* **2010**, *330*, 1078.

(26) Granwehr, J.; Seeley, J. A. *J. Magn. Reson.* **2006**, *179*, 280.

(27) Hilty, C.; McDonnell, E. E.; Granwehr, J.; Pierce, K. L.; Han, S. I.; Pines, A. *Proc. Natl. Acad. Sci. U.S.A.* **2005**, *102*, 14960.

(28) McDonnell, E. E.; Han, S. L.; Hilty, C.; Pierce, K. L.; Pines, A. *Anal. Chem.* **2005**, *77*, 8109.

(29) Harel, E.; Hilty, C.; Koen, K.; McDonnell, E. E.; Pines, A. *Phys. Rev. Lett.* **2007**, *98*.

(30) Harel, E.; Pines, A. *J. Magn. Reson.* **2008**, *193*, 199.

(31) Telkki, V. V.; Hilty, C.; Garcia, S.; Harel, E.; Pines, A. *J. Phys. Chem. B* **2007**, *111*, 13929.

(32) Seeley, J. A.; Han, S. I.; Pines, A. *J. Magn. Reson.* **2004**, *167*, 282.

(33) Harel, E.; Granwehr, J.; Seeley, J. A.; Pines, A. *Nat. Mater.* **2006**, *5*, 321.

(34) Pope, J. M.; Yao, S. *Concepts Magn. Reson.* **1993**, *5*, 281.

(35) Paulsen, J.; Bajaj, V. S.; Pines, A. *J. Magn. Reson.* **2010**, *205*, 196.

(36) Lustig, M.; Donoho, D.; Pauly, J. M. *Magn. Reson. Med.* **2007**, *58*, 1182.

(37) Barrie, P. J. *Annu. Rep. NMR Spectrosc.* **2000**, *41*, 265.

(38) Korringa, J.; Seevers, D. O.; Torrey, H. C. *Phys. Rev.* **1962**, *127*, 1143.

(39) Majumdar, S.; Gore, J. C. *J. Magn. Reson.* **1988**, *78*, 41.

(40) Weisskoff, R. M.; Zuo, C. S.; Boxerman, J. L.; Rosen, B. R. *Magn. Reson. Med.* **1994**, *31*, 601.

(41) Hürlimann, M. D. *J. Magn. Reson.* **1998**, *131*, 232.

(42) Sen, P. N.; Axelrod, S. *J. Appl. Phys.* **1999**, *86*, 4548.

(43) Dunn, K. J. *J. Magn. Reson.* **2002**, *156*, 171.

(44) Audoly, B.; Sen, P. N.; Ryu, S.; Song, Y. Q. *J. Magn. Reson.* **2003**, *164*, 154.

(45) Sun, B.; Dunn, K.-J. *Phys. Rev. E* **2002**, *65*, 051309.

(46) Winkler, M.; Zhou, M.; Bernardo, M.; Endeward, B.; Thomann, H. *Magn. Reson. Imaging* **2003**, *21*, 311.

(47) Watson, A. T.; Chang, C. T. P. *Prog. Nucl. Magn. Reson. Spectrosc.* **1997**, *31*, 343.

(48) Zielinski, L. J. *J. Chem. Phys.* **2004**, *121*, 352.

(49) Washburn, K. E.; Callaghan, P. T. *Phys. Rev. Lett.* **2006**, *97*, 175502.

(50) Fernandez-Pello, A. C. *Proc. Combust. Inst.* **2003**, *29*, 883.

(51) Schwindt, P. D. D.; Knappe, S.; Shah, V.; Hollberg, L.; Kitching, J.; Liew, L. A.; Moreland, J. *Appl. Phys. Lett.* **2004**, *85*, 6409.

(52) Taylor, J. M.; Cappellaro, P.; Childress, L.; Jiang, L.; Budker, D.; Hemmer, P. R.; Yacoby, A.; Walsworth, R.; Lukin, M. D. *Nat. Phys.* **2008**, *4*, 810.